

# Learning High-Dimensional Nonparametric Differential Equations via Multivariate Occupation Kernel Functions

Victor Rielly  
 Dept. of Math + Stats  
 Portland State University  
 victor23@pdx.edu

Kamel Lahouel  
 Translational Genomics  
 klahouel@tgen.org

Ethan Lew  
 Galois, Inc.  
 elew@galois.com

Michael Wells  
 Dept. of Math + Stats  
 Portland State University  
 mlwells@pdx.edu

Vicky Haney  
 Dept. of Math + Stats  
 Portland State University  
 vhaney@pdx.edu

Bruno Jedynak  
 Dept. of Math + Stats  
 Portland State University  
 bruno.jedynak@pdx.edu

June 21, 2023

## Abstract

Learning a nonparametric system of ordinary differential equations (ODEs) from  $n$  trajectory snapshots in a  $d$ -dimensional state space requires learning  $d$  functions of  $d$  variables. Explicit formulations scale quadratically in  $d$  unless additional knowledge about system properties, such as sparsity and symmetries, is available. In this work, we propose a linear approach to learning using the implicit formulation provided by vector-valued Reproducing Kernel Hilbert Spaces. By rewriting the ODEs in a weaker integral form, which we subsequently minimize, we derive our learning algorithm. The minimization problem’s solution for the vector field relies on multivariate occupation kernel functions associated with the solution trajectories. We validate our approach through experiments on highly nonlinear simulated and real data, where  $d$  may exceed 100. We further demonstrate the versatility of the proposed method by learning a nonparametric first order quasilinear partial differential equation.

**keywords:** learning ODEs, occupation kernel, vector-valued RKHS, weak formulation, first order PDEs.

## 1 Introduction

### 1.1 Description of the problem

The task of learning dynamical systems derived from ordinary differential equations has garnered a lot of interest in the past couple of decades. In this framework, we are often provided noisy data from trajectories representative of the dynamics we wish to learn, and we provide a candidate model to describe the dynamics. We present a learning algorithm for the vector field guiding the dynamical system that scales linearly with the dimensionality of the dynamical system’s state space.

### 1.2 Examples of applications

High-dimensional dynamical systems play a crucial role in various domains. For instance, finite difference methods are commonly used to solve partial differential equations (PDEs), resulting in dynamical systems whose dimensionality scales with the PDE’s discretization size [26]. Modeling dynamics in high dimensions has garnered significant interest, with recurrent neural networks and LSTM being popular techniques employed [36]. However, these methods often struggle to generalize to new data, limiting their effectiveness [32]. When

the dynamics can be derived from physical principles, an alternative approach involves modeling them using differential equations, which leads to improved generalization.

### 1.3 State of the art

We select a variety of system identification methods that apply to our relevant class of experiments—techniques that learn system dynamics from snapshots of state with good accuracy, scale to tens or hundreds of state dimensions and are robust to noise. Importantly, we do not consider methods that heavily rely on strong invariants of specific classes of dynamical systems, such as spatial dependence or physics-informed constraints. While these methods can be highly effective for particular classes of problems where such invariants are known or can be assumed, they may not be applicable or may perform poorly in more general settings where such information is not present. Our goal is to develop a system identification technique that applies to systems with noisy data and unknown physics, such as clinical models.

Several methods have been proposed and developed for learning ordinary differential equations from snapshots of trajectories. These methods fall broadly into the following topics: sparse identification of nonlinear dynamics, reduced order models, and deep learning methods. Each of these classes has unique characteristics and features, but none fully satisfies the criteria we aim for, which motivates our proposed approach.

**Sparse Identification of Nonlinear Dynamics (SINDy)** SINDy is a well-developed class of data-driven methods for identifying parsimonious dynamical systems models from trajectories. [4] These methods rely on sparse regression techniques to identify the fewest and most relevant terms in the governing equations from a set of candidate functions. It first constructs a library of candidate functions and then uses sparse regression techniques. SINDy has been successfully extended to various problems, including the identification of PDEs [25], systems with control [5], and demonstrates robustness for sparse and limited data [17, 11].

**Reduced Order Models (ROMs)** Reduced Order Models are a class of methods for simplifying high-dimensional dynamical systems by projecting them onto a lower-dimensional subspace. Dynamic mode decomposition is a data-driven method for extracting spatiotemporal patterns and coherent structures from high-dimensional data generated by dynamical systems. It is useful for systems with periodic or quasi-periodic behavior. [33] eDMD extends DMD to handle nonlinear dynamics by working in a higher-dimensional feature space. [34] eDMD applies the DMD algorithm to a nonlinear transformation of the data, which is typically represented by a set of basis functions or a dictionary of candidate functions.

**Deep Learning Methods** Deep learning methods can be used in conjunction with Reduced Order Models (ROMs) to learn transformations to lower-dimensional subspaces. These methods use deep learning to construct an efficient representation of the dynamical system and to capture nonlinear dynamics [24, 35, 20]. Deep learning methods can also be incorporated into the Sparse Identification of Nonlinear Dynamics (SINDy) framework to identify sparse, interpretable, and predictive models from data [8, 2]. There are also deep learning architectures that have been designed for learning ODEs. Physics-informed neural networks (PINNs), for instance, incorporate known physical laws and principles into the architecture and loss function of a neural network [27, 3, 13] and have been applied successfully to physical systems [7, 6]. This can lead to more accurate and physically consistent predictions. However, the application of PINNs often requires substantial domain knowledge and careful engineering. While PINNs have shown promise in many applications, they are out of scope for this work as we aim to develop methods that do not rely on knowledge of physics-informed constraints *before training*.

### 1.4 Main contributions

We find all these methods lack one thing or another. Many methods for instance learn dynamics in a feature space [19], [3]. This may not always be desired as many physical systems are derived from ordinary differential equations in the sample spaces. Other methods may have poor scaling with the dimensionality of the problem. SINDy [9], for example, scales well with dimensionality in principle, but poorly with the number of library functions. In many cases, the number of library functions grows very quickly with the dimensionality of the

problem. We propose to use a method, the occupation kernel (OCK) algorithm, that learns a dynamical system in the sample space, and which scales linearly with the number of dimensions of the problem. The occupation kernel method was originally presented in [29, 30, 31] as well as in the Youtube video [28]. We contribute to providing an alternative derivation of the algorithm with the help of vector-valued RKHS. We also emphasize the simplicity of the algorithm and demonstrate competitive performance on high-dimensional data, as well as noisy data. Finally, We show that the OCK algorithm is the solution to a weak formulation of the learning problem for differential equations, and provide an example where the weak formulation and the OCK algorithm can be used to learn a nonparametric quasilinear first order PDE.

## 2 Background

### 2.1 Vector valued RKHS

Real-valued RKHS are succinctly described in the supplementary material. Vector-valued RKHSs generalize the real-valued case. The construction is similar. Consider a Hilbert space of functions from  $\mathbb{R}^d$  to  $\mathbb{R}^d$ , also called vector fields. Assume, moreover, that the evaluation functional is continuous. Riesz representation theorem then states that for any  $x, v \in \mathbb{R}^d$ , there exists a unique element in  $\mathbb{H}$ , notated  $K_{x,v}$  such that  $v^T f(x) = \langle f, K_{x,v} \rangle$ . The kernel of  $\mathbb{H}$  is then the  $(d, d)$  matrix where the element  $(i, j)$  at the  $i^{\text{th}}$  row and  $j^{\text{th}}$  column is defined by

$$K_{ij}(x, y) = \langle K_{x, e_i}, K_{y, e_j} \rangle \quad (1)$$

where  $(e_1, \dots, e_d)$  is the natural basis of  $\mathbb{R}^d$ . Let us use (1) to characterize the function  $K_{x,v}$ . We start with  $K_{y, e_j}$  and use the reproducing property as well as the symmetry of the inner product.

$$e_i^T K_{y, e_j}(x) = \langle K_{y, e_j}, K_{x, e_i} \rangle = \langle K_{x, e_i}, K_{y, e_j} \rangle = K_{ij}(x, y) = e_i^T K(x, y) e_j \quad (2)$$

Thus  $K_{y, e_j}(\cdot) = K(\cdot, y) e_j$ , and

$$v^T f(x) = \langle f, K_{x,v} \rangle = \langle f, K(\cdot, x) v \rangle \quad (3)$$

which is the reproducing property for vector-valued RKHS. Applying (3) to the function  $x \mapsto K(x, y) w$ , for  $w \in \mathbb{R}^d$  provides

$$v^T K(x, y) w = \langle K(\cdot, y) w, K(\cdot, x) v \rangle = \langle K(\cdot, x) v, K(\cdot, y) w \rangle \quad (4)$$

Lastly, a useful property of the kernel  $K$  is that  $K(x, y)^T = K(y, x)$ . Indeed,

$$\begin{aligned} K_{ji}(x, y) &= e_j^T K(x, y) e_i = \langle K(\cdot, x) e_j, K(\cdot, y) e_i \rangle \\ &= \langle K(\cdot, y) e_i, K(\cdot, x) e_j \rangle = e_i^T K(y, x) e_j = K_{ij}(y, x) \end{aligned} \quad (5)$$

### 2.2 Linear functionals and occupation kernel functions for vector-valued RKHS

Let  $\mathbb{H}$  be an RKHS of functions from  $\mathbb{R}^d$  to  $\mathbb{R}^d$  with matrix-valued kernel  $K$ . Consider a parametric curve  $[a, b] \rightarrow \mathbb{R}^d$ ,  $t \mapsto x(t)$  and define the functional from  $\mathbb{H}$  to  $\mathbb{R}^d$ ,  $L_x(f) = \int_a^b f(x(t)) dt$ .  $L_x$  is linear. If  $x \mapsto K_{ii}(x, x)$  is continuous for each  $i = 1 \dots d$ , then  $L_x$  is also continuous<sup>1</sup>. For each  $v \in \mathbb{R}^d$ , the occupation kernel function  $L_x^*(v)$  is then the element in  $\mathbb{H}$  uniquely defined by the equation  $v^T L_x(f) = \langle f, L_x^*(v) \rangle$ . Note that for any  $w \in \mathbb{R}^d$

$$\begin{aligned} w^T L_x^*(v)(y) &= \langle L_x^*(v), K(\cdot, y) w \rangle = \langle K(\cdot, y) w, L_x^*(v) \rangle = v^T L_x(K(\cdot, y) w) = \\ &= v^T \int_a^b K(x(t), y) w dt = w^T \left[ \int_a^b K(y, x(t)) dt \right] v \end{aligned} \quad (6)$$

were we have use the property that  $K(x, y)^T = K(y, x)$ . Thus,

$$L_x^*(v) = \left[ \int_a^b K(\cdot, x(t)) dt \right] v \quad (7)$$

---

<sup>1</sup>A derivation is provided in the supplementary material

Also,

$$\begin{aligned} \langle L_x^*(v), L_y^*(w) \rangle &= w^T L_y(L_x^*(v)) = w^T \int_{t=a}^b L_x^*(v)(y(t)) dt \\ &= w^T \left[ \int_a^b \int_{s=a}^b K(y(t), x(s)) ds dt \right] v = v^T \left[ \int_a^b \int_a^b K(x(s), y(t)) ds dt \right] w \end{aligned} \quad (8)$$

## 3 Methods

### 3.1 The occupation kernel (OCK) algorithm

We describe the OCK algorithm in two steps. In the first step, we assume that we observe  $n$  trajectories or curves in  $\mathbb{R}^d$ , the solution of a single ODE, each with a different known initial condition, and we aim at recovering the vector field driving this ODE. Assuming that this vector field belongs to an RKHS, and under a penalized least square loss, we provide a solution expressed in terms of occupation kernel functions. In the second step, we relax the hypothesis and assume that the trajectories are not provided; instead, snapshots along these trajectories are provided. Rearranging these trajectories and replacing the integrals with a numerical quadrature thus provides the proposed numerical solution.

### 3.2 The occupation kernel algorithm from curves

Consider the ODE

$$\dot{x} = f_0(x), x \in \mathbb{R}^d \quad (9)$$

where  $f_0 : \mathbb{R}^d \rightarrow \mathbb{R}^d$  is a fixed, unknown vector field. Consider also  $n$  curves  $x_1(t), \dots, x_n(t)$ , from  $[a_i, b_i]$  to  $\mathbb{R}^d$ . Let us then design an optimization setting, an inverse problem, for recovering  $f_0$  from these trajectories. Let  $H$  be an RKHS of continuous vector-valued functions from  $\mathbb{R}^d$  to  $\mathbb{R}^d$ ,  $\lambda > 0$ , a constant, and let us define the functional,

$$J(f) = \frac{1}{n} \sum_{i=1}^n \left\| \int_{a_i}^{b_i} f(x_i(t)) dt - x_i(b_i) + x_i(a_i) \right\|_{\mathbb{R}^d}^2 + \lambda \|f\|_{\mathbb{H}}^2 \quad (10)$$

Thanks to the fundamental theorem of calculus, the first term is minimized when  $f = f_0$ . However, aside from degenerate cases, this minimizer is not unique. Thus, the second term is a regularization term, minimized when  $f = 0$ . The problem of minimizing (10) over  $H$  is well-posed. It has a unique solution that can be expressed using the occupation kernel functions as follows:

**Theorem 1** *The unique minimizer of  $J$  over the RKHS  $\mathbb{H}$  with kernel  $K$  is*

$$f^* = \sum_{i=1}^n L_{x_i}^*(\alpha_i), \alpha_i \in \mathbb{R}^d \quad (11)$$

where  $L_{x_i}^*$  is the occupation kernel function of the curve  $x_i$  along the interval  $[a_i, b_i]$ , that is

$$L_{x_i}^*(v) = \left[ \int_{a_i}^{b_i} K(\cdot, x_i(t)) dt \right] v \quad (12)$$

and where the vector  $\alpha = (\alpha_1^T, \dots, \alpha_n^T)^T$  is a solution of

$$(L^* + \lambda n I) \alpha = x(b) - x(a), x(a) = (x_1(a_1)^T, \dots, x_n(a_n)^T)^T, x(b) = (x_1(b_1)^T, \dots, x_n(b_n)^T)^T \quad (13)$$

and  $L^*$  is the  $(nd, nd)$  matrix made of  $(d, d)$  blocks, each defined by

$$L_{ij}^* = \int_{t=a_j}^{b_j} \int_{s=a_i}^{b_i} K(x_i(s), x_j(t)) ds dt \quad (14)$$

The proof is a straightforward generalization of the representer theorem in RKHSs. It is presented in the supplementary material.

### 3.3 The occupation kernel algorithm from data

Let us now assume that instead of observing  $n$  curves that are solutions of (9), we observe  $m + 1$  snapshots, sometimes noisy,  $z_j = (z_j^{(0)}, \dots, z_j^{(m)})$  at time-points  $t_0, \dots, t_m$  along each curve  $z_j$ ,  $j = 1 \dots p$ . Firstly, we reshape this data into  $n = mp$  trajectories, each made of two samples. Secondly, we replace the integral in (12) by an integral quadrature, noted  $\oint$ , and the double integral in (14) by a double integral quadrature, noted  $\iint$ . In both cases, we use the trapezoidal rule. The resulting algorithms for learning and inference are presented in Alg. 1 and Alg 2 respectively.

---

#### Algorithm 1 OCK learning algorithm

---

**Require:**  $x$  of format (n,d)  
**for**  $i = 1 \dots n, j = 1 \dots n$  **do**  
 $L_{ij}^* \leftarrow \iint K(x_i(s), x_j(t)) ds dt$   
**end for**  
Solve for  $\alpha$  the linear system  $(L + \lambda n I) \alpha = y$

---



---

#### Algorithm 2 OCK inference algorithm

---

**Require:**  $x$  of format (n,d)  
**Require:**  $z$  of format (p,d) a vector of  $p$  initial conditions  
**for**  $i = 1 \dots n, j = 1 \dots p$  **do**  
 $L_{x_i}^*(\alpha_i)(z_j) \leftarrow [\oint K(z_j, x_i(t)) dt] \alpha_i$   
**end for**  
**for**  $j = 1 \dots p$  **do**  
 $f^*(z_j) \leftarrow \sum_{i=1}^n L_{x_i}^*(\alpha_i)(z_j)$   
**end for**

---

### 3.4 Computational complexity

In practice, we may choose a matrix-valued kernel  $K(x, y)$  that is given by  $K(x, y) = k(x, y) \cdot I$ . This provides a kernel that is diagonal ( $K(x, y)_{i,j} = 0$  for all  $i \neq j$ ). Moreover  $K(x, y)_{i,i} = K(x, y)_{j,j} = k(x, y)$  for all  $i, j$ . In such a case, the linear system 13 becomes equivalent to solving an  $n \times n$  linear system for a  $n \times d$  solution. Therefore, we require  $O(dn^2)$  to construct the gram matrix for a Gaussian kernel,  $O(n^2)$  to estimate the integrals, and  $O(dn^3)$  to solve the linear system. We have a space complexity of  $O(n^2)$ .

On the other hand, if we let  $\psi(x) \in \mathbb{R}^{d \times q}$ , then  $K(x, y) = \psi(x)^T \psi(y) \in \mathbb{R}^{d \times d}$  is a valid kernel for a vector-valued RKHS. In such a case, we get a  $q \times q$  linear system to find  $f$ , and we require  $n, d \times q$  by  $q \times d$  matrix-matrix multiplications to construct the system. This gives us a computational complexity of  $O(dnq^2) + O(q^3)$ . Full details are provided in the supplementary materials.

### 3.5 Weak formulation for ODE learning

A legitimate question consists in asking for the origin of the functional (10). Note that if we had used a probabilistic generative model with a Gaussian process prior and Gaussian noise then the trajectories  $x_i(t)$  in (10) would depend on  $f$  and not on  $f_0$ . Optimization would then be much more challenging. There are solutions, including [18, 15] but none of them scale linearly with the dimension of the state space.

Let us present a weak formulation for learning ODEs that is inherited from the weak formulation used in numerical analysis. Note a fundamental difference: in numerical analysis,  $f$  is given, and the aim is the forward problem of generating trajectories, while here, a collection of trajectories  $x_1, \dots, x_n$  over the intervals  $[a_i, b_i]$  respectively are given, and we aim at inferring  $f$ , that is, solving an inverse problem.

Assume that the initial conditions  $x_i(0)$  are known. Let  $\mathbb{G}$  be an RKHS of continuous curves  $[a, b] \rightarrow \mathbb{R}^d$ .

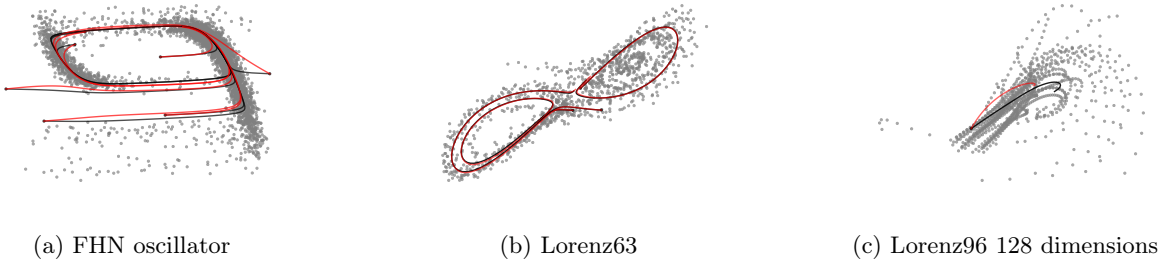


Figure 1: The grey points are the training data. The black curves are the test trajectories. The red curves are the predictions on the test set. For data in dimensions higher than two, only the first two dimensions are shown.

Let us then define the functional

$$Q(f) := \sup_{\Phi_1, \dots, \Phi_n \in \mathbb{G}, \|\Phi_1\|_{\mathbb{G}} = \dots = \|\Phi_n\|_{\mathbb{G}} = 1} \frac{1}{n} \sum_{i=1}^n \left[ \int_{a_i}^{b_i} [\dot{x}_i(t) - f(x_i(t))]^T \Phi_i(t) dt \right]^2 \quad (15)$$

Note that  $Q(f) \geq Q(f_0) = 0$ . The equation  $Q(f) = 0$  is a weak formulation of (9).

Let us now provide an alternate formulation for (15).

**Theorem 2** *Let  $G$  be the matrix-valued kernel of  $\mathbb{G}$ . Then,*

$$Q(f) = \frac{1}{n} \sum_{i=1}^n \int_{a_i}^{b_i} \int_{a_i}^{b_i} [\dot{x}_i(t) - f(x_i(t))]^T G(s, t) [\dot{x}_i(s) - f(x_i(s))] ds dt \quad (16)$$

Moreover, when  $G = I$ , where  $I$  is the  $(d, d)$  identity matrix then (16) simplifies to the data term in (10).

Theorem 2 provides a justification for choosing the loss function (10). It provides also a justification for the OCK algorithm: it is the solution to a weak formulation for learning the ODE (9).

The proof is provided in the supplemental material. It uses the Riesz representation in  $\mathbb{G}$ , the Cauchy-Schwartz inequality, and integration by parts.

## 4 Experiments

### 4.1 Datasets

We test the methods on a diverse set of synthetic and real-world datasets that reflect the challenges of learning systems of ODEs. A summary of the datasets is provided in table 1.  $d$  refers to the number of dimensions of the system,  $n$  the number of trajectories, and  $m$  the average number of samples per trajectory. Training time is in seconds.

**Noisy Fitz-Hugh Nagumo** The FitzHugh-Nagumo oscillator [12] is a nonlinear 2D dynamical system that models the basic behavior of excitable cells, such as neurons and cardiac cells<sup>2</sup>.

**Noisy Lorenz63** The Lorenz63 system [21] is a 3D system provided as a simplified model of atmospheric convection.

**Lorenz96** The Lorenz96 data arises from [22] in which a system of equations is proposed that may be chosen to have any dimension greater than 3.

**CMU Walking** The Carnegie Mellon University (CMU) Walking data is a repository of publicly available data. It can be found at <http://mocap.cs.cmu.edu/>.

**Plasma** This dataset includes imaging and plasma biomarkers from the WRAP study, see [16].

**Imaging** This dataset includes regional imaging biomarkers from the WRAP study, see [16].

<sup>2</sup>Further details of the datasets are provided in the supplementary materials.

Table 1: Datasets

Name	Type	d	n	m	training time(sec)
Noisy Fitz-Hugh Nagumo	Synthetic	2	150	201	40.48
Noisy Lorenz63	Synthetic	3	150	201	31.98
Lorenz96-16	Synthetic	16	100	243	31.12
Lorenz96-32	Synthetic	32	100	243	31.92
Lorenz96-128	Synthetic	128	100	243	31.75
CMU Walking	Real	50	75	106.7	3.63
Plasma	Real	6	425	2.95	0.21
Imaging	Real	117	231	2.26	0.02

Table 2: Methods Considered

Method	Hyperparameters
Null	N/A
<b>Sparse Identification of Nonlinear Dynamics</b>	
SINDy [4]	polynomial degree, sparsity threshold
<b>Reduced Order Models</b>	
eDMD-RFF [10]	number of features, lengthscale
eDMD-Poly [34]	polynomial degree
<b>Deep Learning</b>	
ResNet [14] [23]	network depth/breadth
eDMD-Deep [35]	latent space dimension, autoencoder depth/breadth

For our experiments, we select competitive methods covering various categories, shown in Table 2.<sup>3</sup> All experiments are run in Google colab on default settings. The GPU was only enabled (A100, High-RAM) for the deep learning techniques as the PyTorch neural networks could benefit from them. Lastly, we compare all methods against the null model, which simply predicts no change  $\mathbf{x}(t) = \mathbf{x}_0$ .

## 4.2 Evaluation

Testing consisted of integrating predicted trajectories starting at the initial conditions. We use the loss

$$\text{Err} = \sqrt{\sum_{i=2}^n (t_i - t_{i-1}) \|y_i - \hat{y}_i\|^2} \quad (17)$$

We also used 1-Err, in which  $n = 2$  in (17). All the methods were trained, validated and tested on the same data. For model tuning, we select a small number of values on a log scale for each hyperparameter and run grid search with a 20 percent validation set 2.

Table 3 summarizes the system identification errors for each of the experiments; it is evident that model performance varies significantly across different systems, indicating that no single model consistently outperforms others across all systems. In the Lorenz96-16 and Lorenz96-32 systems, the SINDy polynomial model exhibited substantial performance, with an error magnitude significantly lower than that of its closest competitors. This model was able to closely replicate the underlying Lorenz96 equations. Notably, the eDMD-Deep and OCK models yielded best results for the Lorenz96-128 and CMU experiments. In the case of the ResNet method, the model encountered numerical instabilities and produced NaN values for the plasma and imaging experiment. We anticipate an improvement in the performance of ResNet and eDMD-Deep for high-dimensional systems with abundant trajectory data. In other cases, data sparsity posed a challenge, making it difficult to tune the neural networks for competitive performance.

<sup>3</sup>More details are provided in the supplementary material

Table 3: Dynamical System Estimation Results

Lorenz 63		FHN		Lorenz 96-16		Lorenz 96-32					
Err	1-Err	Err	1-Err	Err	1-Err	Err	1-Err				
do	23***	.18***	do	65***	.85***	do	65***	.098***	do	116***	.197***
ed	31***	.10***	ed	49***	.51**	ed	59***	.400***	ed	88***	.573***
ep	23***	.15***	ep	62***	.53***	ep	63***	.275***	ep	88***	.418***
er	28***	.11***	er	57***	1.5***	er	62***	.294***	er	88***	.422***
n	27***	.13***	n	100***	.56***	n	75***	.395***	n	105***	.559***
sp	14	<b>.03</b>	sp	29**	<b>.34</b>	sp	<b>4</b>	<b>.003</b>	sp	<b>5</b>	<b>.004</b>
ock	<b>13</b>	.04	ock	<b>18</b>	.4	ock	43	.033	ock	82	.08
Lorenz 96-128		Plasma		Imaging		CMU					
Err	1-Err	Err	1-Err	Err	1-Err	Err	1-Err				
do	236***	2.64***	do	NA	NA	do	NA	NA	do	203	8.4
ed	<b>167</b>	.89***	ed	100***	58***	ed	180***	93***	ed	<b>144</b>	18.6***
ep	184***	1.07***	ep	1262***	149***	ep	7e6***	3e6***	ep	206	<b>7.4</b>
er	180***	1.12***	er	90***	54***	er	5e5***	2e5***	er	150	7.4
n	210***	1.12***	n	56*	32	n	100	68	n	202	9.5***
sp	188***	.66***	sp	<b>55</b>	32	sp	1e3***	7e2***	sp	815***	8.7
ock	167	<b>.59</b>	ock	55	<b>32</b>	ock	<b>91</b>	<b>65</b>	ock	236	8.6

**Description:** We run a one sided Wilcoxon comparison test between our model, and all other models. Low  $P$  values indicate our model outperforms. \*\*\* :  $P < .001$ ; \*\* :  $P < .01$ ; \* :  $P < .05$ . Minimum values are in bold. Method types are given as follows: do: resnet; ed: edmd-deep; ep: edmd-poly; er: edmd-rff; n: null; sp: SINDy-poly; ock: occupational kernel. 1-Err is the error over 1 sample trajectory. It should be noted that the Lorenz 96 system is a quadratic system so in the small dimension case SINDy outperforms.

The OCK model demonstrated superior performance for the noisy Lorenz63, Lorenz96-128, plasma, and imaging system experiments. It is important to emphasize the occupation kernel model’s strong performance on real-world datasets, particularly the plasma and imaging. In the Plasma dataset, the SINDy polynomial and occupational kernel models were on par, both exhibiting the lowest error. However, the occupational kernel model demonstrated a slightly superior performance with a better 1-sample trajectory error. In the context of real-world data, the occupation kernel method outperformed the other models, as exemplified by its performance in the imaging data, where it was the only method that surpassed the null model. Figure 2 illustrates a predicted trajectory of imaging biomarkers from the test set of the WRAP study using the occupation kernel method over a 7.7 year time horizon. These results underscore the practical efficacy of the occupation kernel method in handling real-world data.

## 5 Learning a nonparametric quasilinear first order partial differential equation

By means of slight modifications to the proposed algorithm for the ODE setting, it is possible to derive an OCK algorithm to learn nonparametric partial differential equations. In this section, we illustrate our approach for first order quasilinear partial differential equations. Consider the following family of PDEs:

$$\alpha(x)u_x(x, y) + u_y(x, y) = f(u(x, y)) \quad (18)$$

For simplicity, suppose that we observe the solution  $u$  on a uniform grid  $(x_i, y_j)$  over  $x \in [a, b]$ ,  $y \in [c, d]$  with  $i \in \{1, \dots, n\}$  and  $j \in \{1, \dots, m\}$ . We assume  $\alpha \in \mathbb{H}_1$  and  $f \in \mathbb{H}_2$  where  $\mathbb{H}_1$  and  $\mathbb{H}_2$  are two univariate RKHSs, with respective kernels  $k_1$  and  $k_2$ . Similarly to equation 16, we derive a weak formulation of the PDE 18. We fix the solution  $u$  of the PDE. Define  $D_{f,\alpha} : \mathbb{R}^2 \mapsto \mathbb{R}$  as:

$$D_{f,\alpha}(x, y) := \alpha(x)u_x(x, y) + u_y(x, y) - f(u(x, y)) \quad (19)$$

The functional corresponding to the weak formulation of the PDE is then:

$$Q(f, \alpha) = \int_{[a,b] \times [c,d]} \int_{[a,b] \times [c,d]} D_{f,\alpha}(x_1, y_1) D_{f,\alpha}(x_2, y_2) G((x_1, y_1), (x_2, y_2)) dx_1 dy_1 dx_2 dy_2 \quad (20)$$

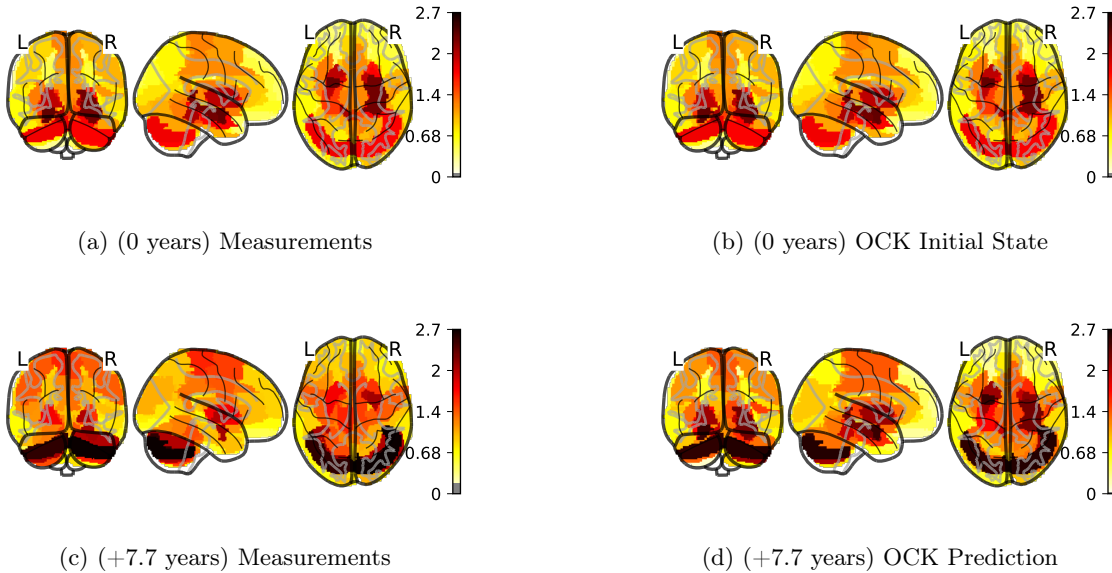


Figure 2: OCK Predicted Biomarker Values

where  $\mathbb{G}$  is a univariate kernel defined on  $\mathbb{R}^2 \times \mathbb{R}^2$ . In this example, we use the explicit kernel defined by the feature maps:

$$\phi_{i,j}(x, y) = \begin{cases} 1 & (x, y) \in [x_i, x_{i+1}] \times [y_j, y_{j+1}] \\ 0 & \text{otherwise} \end{cases} \quad (21)$$

In practice, the integrals defining  $Q(f, \alpha)$  are estimated using the points of the grid where the solution is observed and the trapezoid rule quadrature. Finally, the minimization problem leading to the estimation of  $f$  and  $\alpha$  is:

$$\min_{\alpha \in \mathbb{H}_1, f \in \mathbb{H}_2} \hat{Q}(f, \alpha) + \lambda_1 \|\alpha\|_{\mathbb{H}_1}^2 + \lambda_2 \|f\|_{\mathbb{H}_2}^2. \quad (22)$$

where  $\hat{Q}(f, \alpha)$  is the estimator of  $Q(f, \alpha)$ . Here we have replaced the integral by a quadrature. The minimization problem is solved using the representer theorem in both RKHSs  $\mathbb{H}_1$  and  $\mathbb{H}_2$ . Details of the derivation of the weak formulation 20 and the solution of the minimization problem 22 are provided in the supplementary material.

## 5.1 Experiments with a quasilinear PDE

The algorithm is tested on the example:

$$u(x, y) = \left(1 + e^{y + \sin(4\pi(\arctan(x) - y))}\right)^{-1} \quad (23)$$

which satisfies

$$(1 + x^2)u_x + u_y = -u(1 - u). \quad (24)$$

The solution is observed on uniform grids ranging from  $100 \times 10$  to  $12800 \times 1280$  on the rectangle  $[-4, 4] \times [0, 1]$ . We use random Fourier features [1] with 100 features each for  $\alpha$  and  $f$  to approximate the Gaussian kernel. We report the estimation errors of  $f$  and  $\alpha$  on different resolutions of the grid in the supplementary material.

## 6 Summary and discussion

Thanks to the implicit matrix-valued kernel formulation, we have demonstrated that the OCK algorithm, originally proposed by J. Rosenfeld and co-authors, allows for learning the vector field of an ODE, and

scales linearly with the dimension of the state space. We have compared the algorithm to a representative selection of competitive algorithms. We have shown consistent performance. We have also demonstrated that the OCK algorithm is the solution to a weak formulation of the problem of learning the vector field of an ODE. Following the same line of thought, we have devised a weak formulation for learning a nonparametric quasilinear first-order PDE employing the OCK algorithm.

The weak formulation allows for a more general setting than the cost function provided in (10). In particular, we plan to explore different RKHSs of test functions in (16), including explicit and implicit kernels.

## 7 Acknowledgements

The work at Portland State University (PSU) was partly funded using the National Institute of Health RO1AG021155, R01EY032284, and R01AG027161, and National Science Foundation #2136228. The Google Research award “Kernel PDE” also helped fund the work at PSU and at TGen. The funding sources had no involvement in the study design; in the collection, analysis, and interpretation of data; in the report’s writing; and in the decision to submit the article for publication. The material of Galois, Inc. is based upon work supported by the Air Force Research Laboratory (AFRL) and DARPA under Contract No. FA8750-20-C-0534. Any opinions, findings, conclusions, or recommendations expressed in this material are those of the author(s). They do not necessarily reflect the views of the Air Force Research Laboratory (AFRL) and DARPA.

## A Experiment Code

We created a code capsule on Code Ocean that hosts all the methods used in our experiments for system identification of ordinary differential equations. The code repository allows for the repeatability of our results for a single experiment—Lorenz63—and facilitates the evaluation of the performance of different models on synthetic and real-world datasets. The real world plasma and imaging experiment are restricted data and will not be available for the evaluation.

In accordance with the NeurIPS 2023 code sharing guidelines, we provide an *anonymized* zipfile (6.6 MB) export of the code capsule for review at <https://drive.google.com/file/d/1ug9YhdFHBxYNQNIvj1hS-ZngLwKu-h3a/view?usp=sharing>. The code can be run locally in a Docker container with instructions in the README.md and REPRODUCING.md. After review, we will publish a de-anonymized capsule available on the Code Ocean platform, as well as a public GitHub repository of the code with a detailed README.md covering the Papers with Code release checklist <sup>4</sup>.

To ensure the reproducibility of the experiment, we have tuned the hyperparameters for each method, except for ResNet, which is known to require substantial tuning time. The code repository provides detailed instructions for running each method experiment, including the necessary input data and the corresponding hyperparameter settings. Please note that due to limitations on Code Ocean, we have set the TensorFlow library to use the CPU rather than the GPU, as using the GPU resulted in numerous errors. This may increase the runtime of the experiments. For the paper, we ran some experiments in google colab on A100 GPUs where the training time was much lower.

Upon running the code repository, the experiments will take approximately 1.5 hours to complete. The results of each experiment are provided in the form of trajectory CSV files, capturing the predicted trajectories of the identified systems. These trajectory files can be further analyzed or visualized as desired. Additionally, a summary of the performance of each method is available in the code repository.

## B Datasets

### B.1 Synthetic data

**Noisy Fitz-Hugh Nagumo** The FitzHugh-Nagumo oscillator [12] is a nonlinear 2D dynamical system that models the basic behavior of excitable cells, such as neurons and cardiac cells. The system is popular in the analysis of dynamical systems for its rich behavior, including relaxation oscillations and bifurcations. The

<sup>4</sup><https://github.com/paperswithcode/releasing-research-code>

FHN oscillator consists of two coupled ODEs that describe the membrane potential  $v$  and recovery variable  $w$ . Here,  $I$  is the external current input,  $a$  and  $b$  are positive constants that affect the shape and duration of the action potential, and  $\tau$  is the time constant that determines the speed of the recovery variable’s response. We added random Gaussian noise of standard deviation 0.12 to this dataset.

**Noisy Lorenz63** The 3D Lorenz 63 system [21] is a simplified model of atmospheric convection, but has since become a canonical example of chaos in dynamical systems. The Lorenz 63 system exhibits sensitive dependence on initial conditions and parameters, which gives rise to its characteristic butterfly-shaped chaotic attractor. The equations are

$$\begin{aligned}\frac{dx}{dt} &= \sigma(y - x) \\ \frac{dy}{dt} &= x(\rho - z) - y. \\ \frac{dz}{dt} &= xy - \beta z\end{aligned}\tag{25}$$

Here,  $x$ ,  $y$ , and  $z$  are state variables representing the fluid’s convective intensity, and  $\sigma$ ,  $\rho$ , and  $\beta$  are positive parameters representing the Prandtl number, the Rayleigh number, and a geometric factor, respectively. We added random Gaussian noise with standard deviation 0.5 to this dataset.

**Lorenz96** The Lorenz96 data arises from [22] in which a system of equations is proposed that may be chosen to have any dimension greater than 3. The chaotic system is defined by:

$$\frac{dx_k}{dt} = -x_{k-1}x_{k-1} + x_{k+1}x_{k-1} - x_k + F\tag{26}$$

where we take  $F = 8$  and consider 16, 32 and 128 dimensional systems. Indices are assumed to wrap so that for an  $n$  dimensional system  $x_{-2} = x_{n-2}$ .

## B.2 Real Data

**CMU Walking** The Carnegie Mellon University (CMU) Walking data is a repository of publicly available data. It can be found at <http://mocap.cs.cmu.edu/>. It was generated by placing sensors on a number of subjects and recording the position of the sensors as the subjects walked forward by a fixed amount and then walked back. There were 50 spatial dimensions of data as recorded by the sensors, which were recorded at regular times. Since the observation times were not provided, we separated each observation in time by 0.1 units and began each trajectory at time zero. The CMU Walking data which we used for our experiments consists of 75 trajectories with an average of 106.7 observations per trajectory. We could not use the full amount of data provided because some subjects did not walk in the same manner as other subjects.

It should be noted that it may not be appropriate to consider the CMU walking data as being generated by a single dynamical system. Since there were multiple subjects in the dataset, it is reasonable to conclude that there are multiple dynamical systems responsible for the motion of these different subjects. However, we fit our model to this dataset assuming that it was generated by a single dynamical system.

**Plasma** This dataset includes imaging and plasma biomarkers from the WRAP study, see [16]. The imaging biomarker is a distribution volume ratio obtained from Pittsburgh Compound-B positron emission tomography. The plasma biomarkers include  $A\beta_{40}/A\beta_{42}$  that reflects specific amyloid beta ( $A\beta$ ) proteoforms; ptau217, which has a high correlation with amyloid PET positivity, GFAP, which measures the levels of the astrocytic intermediate filament glial fibrillary acidic protein, and NFL, a recognized biomarker of subcortical large-caliber axonal degeneration, for a total of 6 biomarkers. There are a total  $n = 425$  trajectories, one per subject, and, on average, 2.95 time points per trajectory. The data was split (70%, 10%, 20%) corresponding resp. to training, validation, and testing.

**Imaging** This dataset includes regional imaging biomarkers from the WRAP study, see [16]. The imaging biomarker is an atlas-based distribution volume ratio obtained from Pittsburgh Compound-B positron emission tomography. There are a total of 117 biomarkers. There are a total  $n = 231$  trajectories, one per subject, and, on average, 2.26 time points per trajectory. The data was split (70%, 10%, 20%) corresponding resp. to training, validation, and testing.

## C Computational Complexity

Note that the running time mentioned in the paper in Table 1 corresponds to the OCK algorithm. We detail below an analysis of the complexity in terms of  $d$ , the dimension of the state space, and  $n$ , the total number of observations.

### C.1 Implicit kernel

In our experiments, an implicit Gaussian kernel was used. The Gram matrix for the kernel is  $n \times m$  where  $n$  is the total number of samples in the dataset  $X$  and  $m$  is the total number of samples in the dataset  $Y$ . If  $X \in \mathbb{R}^{d \times n}$ , and  $Y \in \mathbb{R}^{d \times m}$ , we may compute any radial basis function kernel defined by:

$$G_{i,j} = f(\|x_i - y_j\|^2) \quad (27)$$

by observing:

$$D = \text{outer}(\text{sum}(X \otimes X), 1_m) - 2X^T Y + \text{outer}(1_n, \text{sum}(Y \otimes Y)) \quad (28)$$

Where  $D_{i,j} = \|X_i - Y_j\|^2$  is the matrix of square distances,  $\otimes$  is the Hadamard product, *sum* is column sum, *outer* is an outer product, and  $1_n$  is the ones vector in  $n$  dimensions.  $G \in \mathbb{R}^{n \times n}$  is then calculated by applying  $f$  component by component to  $D$  for the training set  $X$  with  $X$ . The computational bottleneck of this Gram matrix computation is the  $n \times d$  by  $d \times m$  matrix matrix multiplication, with a worst case run time that is  $O(dnm) = O(dn^2)$  when  $Y = X$  (with a naive implementation of matrix matrix multiplication).

We integrate over intervals of a single pair of samples, and these integrals are estimated using the trapezoid rule quadrature. Therefore, for instance, if a single trajectory is given, we would get our estimate of all our integrals by simply taking the kernel

$$k = \frac{h^2}{4} \begin{bmatrix} 1 & 1 \\ 1 & 1 \end{bmatrix} \quad (29)$$

and convolving it with the Gram matrix  $G$ . If multiple trajectories are given, we apply the same convolution to  $G$  and ignore terms involving sums that mix samples from different trajectories. In Numpy indexing notation, we may apply the above convolution with the expression:

$$M = \frac{h^2}{4} (G[1 :, 1 :] + G[:, -1, 1 :] + G[1 :, :, -1] + G[:, -1, :, -1]) \quad (30)$$

This adds an additional  $O(n^2)$  computational complexity (for fixed  $G \in \mathbb{R}^{n \times n}$ ).

Finally, the linear system we solve is:

$$(M + \lambda I) A = Y \quad (31)$$

Where  $M \in \mathbb{R}^{n \times n}$  and  $A, Y \in \mathbb{R}^{n \times d}$ , which adds the dominating computational complexity term of  $O(dn^3)$ .

### C.2 Explicit Kernel

Assuming the vector valued RKHS has a matrix valued kernel of the form

$$K(x, y) = \psi(x)\psi^T(y) \quad (32)$$

where

$$\psi : \mathbb{R}^d \rightarrow \mathbb{R}^{d \times q} \quad (33)$$

we may recall:

$$f(x) = \sum_i \int_{a_i}^{b_i} \psi(x) \psi(x_i(\tau))^T d\tau \alpha_i = \psi(x) \sum_i \int_{a_i}^{b_i} \psi(x_i(\tau))^T d\tau \alpha_i = \psi(x) \beta \quad (34)$$

where  $\beta \in \mathbb{R}^q$  is defined by  $\beta = \sum_i \int_{a_i}^{b_i} \psi(x_i(\tau))^T d\tau \alpha_i$ . Letting

$$\Psi \in \mathbb{R}^{nd \times q} \quad (35)$$

be defined by:

$$\Psi_i \in \mathbb{R}^{d \times q} = \int_{a_i}^{b_i} \psi(x_i(\tau)) d\tau \quad (36)$$

we may observe that

$$L^* = \Psi \Psi^T \quad (37)$$

and

$$\alpha^T L^* \alpha = \beta^T \beta \quad (38)$$

Thus, we reduce the minimization problem 63 to

$$\min_{\beta} J(\beta) = \frac{1}{n} \sum_{i=1}^n \|\Psi \beta\|_i - x_i(b_i) + x_i(a_i)\|_{\mathbb{R}^d}^2 + \lambda \beta^T \beta \quad (39)$$

This simplifies to

$$(\Psi^T \Psi + \lambda I) \beta = \Psi^T y \quad (40)$$

where  $y \in \mathbb{R}^{nd}$  with  $y_i \in \mathbb{R}^d$  and  $y_i = x_i(b_i) - x_i(a_i)$ . Thus, in the explicit kernel case, we require evaluating  $\Psi$  which is  $O(ndq)$ , a  $q \times nd$  by  $nd \times q$  matrix matrix multiplication  $O(q^2(nd))$  and a  $q \times q$  linear system solve which is  $O(q^3)$ . Notice, in the explicit kernel case, no assumptions on the overall structure of the kernel matrix  $K(x, y)$  are needed. For instance, the matrices no longer need to be diagonal or proportional to the identity matrix. However, in practice, for best results,  $q$  will typically be dependent on the dimension  $d$  and the sample size.

## D Reproducing Kernel Hilbert Spaces (RKHS)

Basic notions and notations associated with RKHS are important for understanding the algorithms presented in this paper. We thus provide a short presentation. We limit ourselves to RKHS over the field of real numbers. RKHS are Hilbert spaces for which the evaluation functional is continuous. The evaluation functional at  $x \in \mathbb{R}$  is a mapping from a RKHS  $H$  to  $\mathbb{R}$ , which associates to a function its evaluation at  $x$ , that is  $f \mapsto f(x)$ . Thanks to the Riesz representation theorem, evaluating a function in an RKHS is a geometric operation consisting in computing an inner product. Effectively, There is a unique vector  $k_x \in H$  such that  $f(x) = \langle f, k_x \rangle$ . Moreover, let us define, for any  $x, y \in \mathbb{R}$ , the so-called kernel  $k(x, y) = \langle k_x, k_y \rangle$ . Let us use this to characterize the function  $k_x$ . Evaluating  $k_x$  at  $y$  and using Riesz representation provides  $k_x(y) = \langle k_x, k_y \rangle = \langle k_y, k_x \rangle = k(y, x)$ . Thus the function  $k_x(\cdot)$  is the function  $k(\cdot, x)$ . Thus for any  $f \in H$ ,  $f(x) = \langle f, k(\cdot, x) \rangle$ . This is the reproducible property of the kernel. Applying this property to  $k_y$  implies that  $k(x, y) = \langle k(\cdot, x), k(\cdot, y) \rangle$

### D.1 Linear functionals and occupation kernels

Let  $H$  be an RKHS of functions from  $\mathbb{R}$  to  $\mathbb{R}$  with kernel  $k$ . Assume that  $x \mapsto k(x, x)$  is continuous. Consider a continuous parametric curve  $[0, 1] \rightarrow \mathbb{R}$ ,  $t \mapsto x(t)$  and define the functional from an RKHS  $H$  to  $\mathbb{R}$ ,

$L_x(f) = \int_0^1 f(x(t))dt$ .  $L_x$  is clearly linear. Thanks to the Cauchy-Schwarz inequality,  $L_x$  is bounded. Indeed,

$$|L_x(f)| = \left| \int_0^T f(x(t))dt \right| \quad (41)$$

$$= \left| \int_0^T \langle f, k(\cdot, x(t)) \rangle dt \right| \quad (42)$$

$$\leq \int_0^T |\langle f, k(\cdot, x(t)) \rangle| dt \quad (43)$$

$$\leq \int_0^T \|f\| \|k(\cdot, x(t))\| dt \quad (44)$$

$$= \|f\| \int_0^T \sqrt{k(x(t), x(t))} dt \quad (45)$$

where we have used the Cauchy-Schwarz inequality in (44). Now, since  $t \mapsto x(t)$  and  $x \mapsto k(x, x)$  are continuous, the integral in (45) is upper-bounded. Thus the functional  $L_x(f)$  is continuous.

We thus define, thanks once more to the Riesz representation theorem, the occupation kernel function as the unique element  $L_x^*$  in  $H$  that verifies  $L_x(f) = \langle f, L_x^* \rangle$ . Note that

$$L_x^*(y) = \langle L_x^*, k(\cdot, y) \rangle = \langle k(\cdot, y), L_x^* \rangle = L_x(k(\cdot, y)) = \int_0^1 k(x(t), y) dt \quad (46)$$

Furthermore,

$$\langle L_x^*, L_y^* \rangle = L_y(L_x^*) = \int_0^1 L_x^*(y(t)) dt = \int_0^1 \int_0^1 k(x(s), y(t)) ds dt \quad (47)$$

## D.2 Verifying the continuity for the occupation kernel in multiple dimensions

$(e_1, \dots, e_d)^T$  is the standard basis of  $\mathbb{R}^d$ .

$$|e_j^T L_x(f)| = \left| \int_0^T e_j^T f(x(t)) dt \right| \quad (48)$$

$$\leq \int_0^T |e_j^T f(x(t))| dt \quad (49)$$

$$= \int_0^T |\langle f, K(\cdot, x(t)) e_j \rangle| dt \quad (50)$$

$$\leq \|f\| \int_0^T \sqrt{K_{jj}(x(t), x(t))} dt \quad (51)$$

where we have used the Cauchy-Schwarz inequality. Since  $t \mapsto x(t)$  is continuous, if moreover  $x \mapsto K_{jj}(x, x)$  is continuous for each  $j = 1 \dots d$ , then for each  $x$  and each  $1 \leq j \leq d$ ,  $e_j^T L_x$  is bounded which implies that  $L_x$  is bounded and thus continuous.

## E Proof of Theorem 1

Consider the linear span of the occupation kernel functions  $L_{x_i}^*, i = 1 \dots n$

$$\mathcal{F} = \{f \in \mathbb{H}, f = \sum_{i=1}^n L_{x_i}^*(\alpha_i), \alpha = (\alpha_1, \dots, \alpha_n) \in \mathbb{R}^{dn}\} \quad (52)$$

Note that  $\mathcal{F}$  is linear and finite-dimensional; thus, it is a closed linear subspace of  $\mathbb{H}$ . We can then project any function in  $\mathbb{H}$  orthogonally onto it

$$f = f_{\mathcal{F}} + f_{\mathcal{F}^\perp} \quad (53)$$

Now, for each  $i = 1 \dots n$ , and  $v \in \mathbb{R}^d$ ,

$$v^T \int_{a_i}^{b_i} f(x_i(t)) dt = v^T L_{x_i}(f) = \langle L_{x_i}^*(v), f \rangle = \langle L_{x_i}^*(v), f_{\mathcal{F}} + f_{\mathcal{F}^\perp} \rangle = \langle L_{x_i}^*(v), f_{\mathcal{F}} \rangle \quad (54)$$

where the previous to last equality comes from the fact that  $f_{\mathcal{F}^\perp}$  is perpendicular to  $L_{x_i}^*(v)$ . Thus,

$$\int_{a_i}^{b_i} f(x_i(t)) dt = L_{x_i}(f_{\mathcal{F}}) \quad (55)$$

Next, using the Pythagorean equality

$$\|f\|^2 = \|f_{\mathcal{F}}\|^2 + \|f_{\mathcal{F}^\perp}\|^2 \geq \|f_{\mathcal{F}}\|^2 \quad (56)$$

Thus, for any  $f \in \mathbb{H}$ ,  $J(f_{\mathcal{F}}) \leq J(f)$  which proves that the minimum of  $J$  actually belongs to  $\mathcal{F}$ . Moreover, note that

$$\begin{aligned} \|f_{\mathcal{F}}\|^2 &= \left\langle \sum_{i=1}^n L_{x_i}^*(\alpha_i), \sum_{i=1}^n L_{x_i}^*(\alpha_i) \right\rangle = \sum_{i,j=1}^n \langle L_{x_i}^*(\alpha_i), L_{x_j}^*(\alpha_j) \rangle \\ &= \sum_{i,j=1}^n \alpha_i^T \left[ \int_{a_i}^{b_i} \int_{a_j}^{b_j} K(x_i(s), x_j(t)) ds dt \right] \alpha_j = \sum_{i,j=1}^n \alpha_i^T L_{ij}^* \alpha_j = \alpha^T L^* \alpha \end{aligned} \quad (57)$$

Also,

$$L_{x_i}(f_{\mathcal{F}}) = L_{x_i} \left( \sum_{j=1}^n L_{x_j}^*(\alpha_j) \right) \quad (58)$$

$$= \int_{a_i}^{b_i} \sum_{j=1}^n L_{x_j}^*(\alpha_j)(x_i(t)) dt \quad (59)$$

$$= \sum_{j=1}^n \left[ \int_{a_i}^{b_i} \int_{a_j}^{b_j} K(x_i(t), x_j(s)) ds dt \right] \alpha_j \quad (60)$$

$$= \sum_{j=1}^n L_{ij}^* \alpha_j \quad (61)$$

$$= [L^* \alpha]_i \quad (62)$$

The minimization problem in  $f$  is thus equivalent to minimizing in  $\alpha$

$$J(\alpha) = \frac{1}{n} \sum_{i=1}^n \|[L^* \alpha]_i - x_i(b_i) + x_i(a_i)\|_{\mathbb{R}^d}^2 + \lambda \alpha^T L^* \alpha \quad (63)$$

or equivalently,

$$J(\alpha) = \frac{1}{n} \|L^* \alpha - x(b) + x(a)\|_{\mathbb{R}^{nd}}^2 + \lambda \alpha^T L^* \alpha \quad (64)$$

since  $\lambda > 0$  and  $L^*$  is psd, this is solved by

$$(L^* + \lambda n I) \alpha = x(b) - x(a) \quad (65)$$

## F Proof of Theorem 2

We assume that  $t \mapsto x_i(t)$ , and  $x \mapsto f_0(x)$  are continuous. We also assume that  $x \mapsto f(x)$  are continuous for all  $f \in \mathbb{H}$ . Let us notate

$$h_i(t) = \dot{x}_i(t) - f(x_i(t)) \quad (66)$$

and consider the linear functional

$$L_{f,i}(\Phi_i) = \int_{a_i}^{b_i} h_i(t)^T \Phi_i(t) dt \quad (67)$$

Let us check that  $L_{f,i}$  is bounded.

$$|L_{f,i}(\Phi_i)| \leq \int_{a_i}^{b_i} |h_i(t)^T \Phi_i(t)| dt \quad (68)$$

$$= \int_{a_i}^{b_i} |\langle \Phi_i, G(\cdot, t) h_i(t) \rangle| dt \quad (69)$$

$$\leq \|\Phi_i\|_{\mathbb{G}} \int_{a_i}^{b_i} \|G(\cdot, t) h_i(t)\|_{\mathbb{G}} dt \quad (70)$$

$$= \|\Phi_i\|_{\mathbb{G}} \int_{a_i}^{b_i} \sqrt{h_i(t)^T G(t, t) h_i(t)} dt \quad (71)$$

The hypothesis is enough to guarantee that  $t \mapsto \sqrt{h_i(t)^T G(t, t) h_i(t)}$  is continuous over  $[a_i, b_i]$  and thus integrable.

Now, using Riesz representation theorem, there exists  $L_{f,i}^* \in \mathbb{G}$  such that

$$L_{f,i}(\Phi) = \langle \Phi, L_{f,i}^* \rangle \quad (72)$$

Moreover,

$$v^T L_{f,i}^*(s) = \langle G(\cdot, s) v, L_{f,i}^* \rangle = L_{f,i}(G(\cdot, s) v) = \left[ \int_{a_i}^{b_i} h_i(t)^T G(t, s) dt \right] v = v^T \left[ \int_{a_i}^{b_i} G(s, t) h_i(t) dt \right] \quad (73)$$

thus,

$$L_{f,i}^*(\cdot) = \int_{a_i}^{b_i} G(\cdot, t) h_i(t) dt \quad (74)$$

and

$$\|L_{f,i}^*\|_{\mathbb{G}}^2 = \langle L_{f,i}^*, L_{f,i}^* \rangle = L_{f,i}(L_{f,i}^*) = \int_{a_i}^{b_i} h_i(t)^T L_{f,i}^*(t) dt = \iint_{a_i}^{b_i} h_i(s)^T G(s, t) h_i(t) ds dt \quad (75)$$

Now,

$$Q(f) = \sup_{\Phi_1, \Phi_n, \|\Phi_1\|_{\mathbb{G}} = \dots = \|\Phi_n\|_{\mathbb{G}} = 1} \frac{1}{n} \sum_{i=1}^n \left[ \langle \Phi_i, L_{f,i}^* \rangle_{\mathbb{G}} \right]^2 \quad (76)$$

which is maximized when  $\Phi_i$  is proportional to  $L_{f,i}^*$ , and we obtain

$$Q(f) = \frac{1}{n} \sum_{i=1}^n \|L_{f,i}^*\|_{\mathbb{G}}^2 \quad (77)$$

Now, in the case where  $G(s, t) = I$ , the  $(d, d)$  identity matrix,

$$\|L_{f,i}^*\|_{\mathbb{G}}^2 = \left\| \int_{a_i}^{b_i} (x_i(t) - f(x_i(t))) dt \right\|_{\mathbb{R}^d}^2 = \left\| \int_{a_i}^{b_i} f(x_i(t)) dt - x_i(b_i) + x_i(a_i) \right\|_{\mathbb{R}^d}^2 \quad (78)$$

## G Weak formulation for the quasilinear PDE

### G.1 Weak formulation minimization

Consider the PDE

$$\alpha(x) u_x + u_y = f(u) \quad (79)$$

Let  $\mathbb{G}$  be an RKHS of test functions with associated kernel function  $G(\cdot, \cdot) : \mathbb{R}^2 \times \mathbb{R}^2 \rightarrow \mathbb{R}$ . Let  $\Omega$  be a compact set in  $\mathbb{R}^2$ . From now on, we will assume that  $u \in \mathcal{C}^1(\Omega)$ ,  $x \rightarrow f(x)$  and  $x \rightarrow \alpha(x)$  are continuous. Define:

$$D_{f,\alpha}(x, y) := \alpha(x)u_x(x, y) + u_y(x, y) - f(u(x, y)) \quad (80)$$

and define

$$Q(f, \alpha) = \sup_{\Phi \in \mathbb{G}, \|\Phi\|=1} \left( \int_{\Omega} D_{f,\alpha}(x, y)\Phi(x, y)dxdy \right)^2 \quad (81)$$

Notice that the linear functional:

$$L_{f,\alpha}(\phi) := \int_{\Omega} D_{f,\alpha}(x, y)\Phi(x, y)dxdy \quad (82)$$

is bounded with a norm bounded by

$$\int_{\Omega} |D_{f,\alpha}(x, y)|\sqrt{G((x, y), (x, y))}dxdy \quad (83)$$

and therefore is continuous. Hence, there exists a function  $L_{f,\alpha}^* \in \mathbb{G}$  such that:

$$L_{f,\alpha}(\phi) = \langle L_{f,\alpha}^*, \phi \rangle \quad (84)$$

and

$$L_{f,\alpha}^*(u, v) = \int_{\Omega} D_{f,\alpha}(x, y)G((x, y), (u, v))dxdy \quad (85)$$

Using Cauchy-Schwartz inequality, we conclude that:

$$Q(f, \alpha) = \|L_{f,\alpha}^*(u, v)\|^2 = \int_{\Omega \times \Omega} D_{f,\alpha}(x_1, y_1)D_{f,\alpha}(x_2, y_2)G((x_1, y_1), (x_2, y_2))dx_1dy_1dx_2dy_2 \quad (86)$$

It should be noted that if  $G$  is an explicit kernel, then just as in the case with ODEs, this term simplifies. Assume  $G((x_1, y_1), (x_2, y_2)) = \phi(x_1, y_1)^T \phi(x_2, y_2)$  where  $\phi : \mathbb{R}^2 \rightarrow \mathbb{R}^{nm}$ . Then

$$Q(f, \alpha) = \left\| \int_{\Omega} (\alpha(x)u_x + u_y - f(u))\phi(x, y)dxdy \right\|_{\mathbb{R}^{nm}}^2 = \sum_{i,j} \left( \int_{\Omega} (\alpha(x)u_x + u_y - f(u))\phi_{i,j}dxdy \right)^2 \quad (87)$$

## G.2 Weak formulation minimization numerical solution

Assuming  $\mathbb{H}_1$  and  $\mathbb{H}_2$  are two RKHSs with kernels  $k_1$  and  $k_2$  respectively, We minimize:

$$\min_{\alpha \in \mathbb{H}_1, f \in \mathbb{H}_2} \{J(f, \alpha) = Q(f, \alpha) + \lambda_1 \|\alpha\|^2 + \lambda_2 \|f\|^2\} \quad (88)$$

assuming:

$$\phi_{i,j}(x, y) = \begin{cases} 1 & (x, y) \in [x_i, x_{i+1}] \times [y_j, y_{j+1}] \\ 0 & \text{otherwise} \end{cases} \quad (89)$$

as follows:

$$J(f, \alpha) = \sum_{i,j} \left( \int_{\Omega} (\alpha(x)u_x + u_y - f(u))\phi_{i,j}dxdy \right)^2 + \lambda_1 \|\alpha\|^2 + \lambda_2 \|f\|^2 \quad (90)$$

$$= \sum_{i,j} \left( \int_{x_i}^{x_{i+1}} \int_{y_j}^{y_{j+1}} (\alpha(x)u_x + u_y - f(u))dxdy \right)^2 + \lambda_1 \|\alpha\|^2 + \lambda_2 \|f\|^2 \quad (91)$$

We use the trapezoid rule and fundamental theorem of calculus to estimate the integral:

$$\int_{x_i}^{x_{i+1}} \int_{y_j}^{y_{j+1}} u_y dxdy \approx \frac{h}{2} (u(x_i, y_{j+1}) + u(x_{i+1}, y_{j+1}) - u(x_i, y_j) - u(x_{i+1}, y_j)) \equiv z_{i,j} \quad (92)$$

and we observe

$$\mathcal{L}_{i,j,u}(\alpha) \equiv \int_{x_i}^{x_{i+1}} \int_{y_j}^{y_{j+1}} \alpha(x) u_x dx dy \quad (93)$$

is a linear functional of  $\alpha$ . Similarly

$$\mathcal{M}_{i,j,u}(f) \equiv \int_{x_i}^{x_{i+1}} \int_{y_j}^{y_{j+1}} f(u) dx dy \quad (94)$$

is a linear functional of  $f$ .

Since  $u_x$  is continuous, and assuming that the kernels  $k_1$  and  $k_2$  continuous we demonstrate that these linear functionals are bounded:

$$|\mathcal{L}_{i,j,u}(\alpha)|^2 = \left| \int_{x_i}^{x_{i+1}} \int_{y_j}^{y_{j+1}} \alpha(x) u_x dx dy \right|^2 \quad (95)$$

$$\leq \int_{x_i}^{x_{i+1}} \int_{y_j}^{y_{j+1}} (\alpha(x))^2 dx dy \int_{x_i}^{x_{i+1}} \int_{y_j}^{y_{j+1}} u_x^2 dx dy \quad (96)$$

$$\leq C_1 \int_{x_i}^{x_{i+1}} \int_{y_j}^{y_{j+1}} (\alpha(x))^2 dx dy \quad (97)$$

$$= C_1 \int_{x_i}^{x_{i+1}} \int_{y_j}^{y_{j+1}} (\langle \alpha, k_1(\cdot, x) \rangle)^2 dx dy \quad (98)$$

$$= C_1 \int_{x_i}^{x_{i+1}} \int_{y_j}^{y_{j+1}} \|\alpha\|^2 \|k_1(\cdot, x)\|^2 dx dy \quad (99)$$

$$= C_1 \|\alpha\|^2 \sup_u \|k_1(\cdot, u)\|^2 \int_{x_i}^{x_{i+1}} \int_{y_j}^{y_{j+1}} dx dy \quad (100)$$

$$\leq C \|\alpha\|^2 \quad (101)$$

Similarly,

$$|\mathcal{M}_{i,j,u}(f)|^2 = \left| \int_{x_i}^{x_{i+1}} \int_{y_j}^{y_{j+1}} f(u) dx dy \right|^2 \quad (102)$$

$$= \left| \int_{x_i}^{x_{i+1}} \int_{y_j}^{y_{j+1}} \langle f, k_2(\cdot, u) \rangle dx dy \right|^2 \quad (103)$$

$$= \left| \left\langle f, \int_{x_i}^{x_{i+1}} \int_{y_j}^{y_{j+1}} k_2(\cdot, u) dx dy \right\rangle \right|^2 \quad (104)$$

$$\leq \|f\|^2 \left\| \int_{x_i}^{x_{i+1}} \int_{y_j}^{y_{j+1}} k_2(\cdot, u) dx dy \right\|^2 \quad (105)$$

$$\leq C_2 \|f\|^2 \quad (106)$$

Therefore, there exist elements  $L_{i,j,u}^* \in \mathbb{H}_1$  and  $M_{i,j,u}^* \in \mathbb{H}_2$  respectively for which

$$\mathcal{M}_{i,j,u}(f) = \langle f, M_{i,j,u}^* \rangle, \quad \mathcal{L}_{i,j,u}(\alpha) = \langle \alpha, L_{i,j,u}^* \rangle \quad (107)$$

and

$$J(f, \alpha) = \sum_{i,j} (\langle \alpha, L_{i,j,u}^* \rangle - \langle f, M_{i,j,u}^* \rangle + z_{i,j})^2 + \lambda_1 \|\alpha\|^2 + \lambda_2 \|f\|^2 \quad (108)$$

Finally, we use the representer theorem for  $\alpha$  and  $f$  to conclude that the minimizer of  $J$  with respect to  $f$  and  $\alpha$  may be found in the span of  $M_{i,j,u}^*$  and  $L_{i,j,u}^*$  respectively. Thus, this is a linear regression problem with the solution:

$$\alpha(s) = \sum_{i,j} \alpha_{i,j} \mathcal{L}_{i,j,u}^*(s) \quad (109)$$

$$\mathcal{L}_{i,j,u}^*(s) = \int_{x_i}^{x_{i+1}} \int_{y_j}^{y_{j+1}} k_1(s, x) u_x dx dy \quad (110)$$

$$f(z) = \sum_{i,j} \beta_{i,j} M_{i,j,u}^*(z) \quad (111)$$

where

$$M_{i,j}^*(z) = \int_{x_i}^{x_{i+1}} \int_{y_j}^{y_{j+1}} k_2(z, u(x, y)) dx dy \quad (112)$$

and

$$y_{i,j} = \int_{x_i}^{x_{i+1}} \int_{y_j}^{y_{j+1}} u_y dx dy. \quad (113)$$

Finally, the coefficients  $\alpha, \beta \in \mathbb{R}^{nm}$  are found by minimizing:

$$C(\alpha, \beta) := \|L\alpha - M\beta + y\|^2 + \lambda_1 \alpha^T L\alpha + \lambda_2 \beta^T M\beta \quad (114)$$

With  $M, L \in \mathbb{R}^{nm \times nm}$  defined by:

$$L_{i,j,k,l} = \int_{x_i}^{x_{i+1}} \int_{y_j}^{y_{j+1}} \int_{x_k}^{x_{k+1}} \int_{y_l}^{y_{l+1}} k_1(s, x) u_s u_x ds dz dx dy \quad (115)$$

$$M_{i,j,k,l} = \int_{x_i}^{x_{i+1}} \int_{y_j}^{y_{j+1}} \int_{x_k}^{x_{k+1}} \int_{y_l}^{y_{l+1}} k_2(u(s, z), u(x, y)) ds dz dx dy \quad (116)$$

### G.3 Numerical minimization with Explicit Kernels

Let us assume  $k_1(x, y) = \psi_1(x)^T \psi_1(y)$  and  $k_2(u, z) = \psi_2(u)^T \psi_2(z)$  with  $\psi_1(x) \in \mathbb{R}^{p_1}$  and  $\psi_2(x) \in \mathbb{R}^{p_2}$  then,

$$\alpha(s) = \sum_{i,j} \alpha_{i,j} \int_{x_i}^{x_{i+1}} \int_{y_j}^{y_{j+1}} \psi_1(s)^T \psi_1(x) u_x dx dy \quad (117)$$

$$= \psi_1(s)^T \left( \sum_{i,j} \alpha_{i,j} \int_{x_i}^{x_{i+1}} \int_{y_j}^{y_{j+1}} \psi_1(x) u_x dx dy \right) \quad (118)$$

$$(119)$$

and

$$f(z) = \sum_{i,j} \beta_{i,j} \int_{x_i}^{x_{i+1}} \int_{y_j}^{y_{j+1}} \psi_2(z)^T \psi_2(u) dx dy \quad (120)$$

$$= \psi_2(z)^T \left( \sum_{i,j} \beta_{i,j} \int_{x_i}^{x_{i+1}} \int_{y_j}^{y_{j+1}} \psi_2(u) dx dy \right) \quad (121)$$

As before, we may define:

$$\gamma \equiv \sum_{i,j} \alpha_{i,j} \int_{x_i}^{x_{i+1}} \int_{y_j}^{y_{j+1}} \psi_1(x) u_x dx dy \quad (122)$$

$$\delta \equiv \sum_{i,j} \beta_{i,j} \int_{x_i}^{x_{i+1}} \int_{y_j}^{y_{j+1}} \psi_2(u) dx dy \quad (123)$$

Then

$$\alpha(s) = \psi_2(s)^T \gamma \quad (124)$$

$$f(z) = \psi_2(z)^T \delta \quad (125)$$

Defining  $\Psi_1 \in \mathbb{R}^{p_1 \times nm}$  and  $\Psi_2 \in \mathbb{R}^{p_2 \times nm}$  with

$$(\Psi_1)_{i,j} = \int_{x_i}^{x_{i+1}} \int_{y_j}^{y_{j+1}} \psi_1(x) u_x dx dy \in \mathbb{R}^{p_1} \quad (126)$$

and

$$(\Psi_2)_{i,j} = \int_{x_i}^{x_{i+1}} \int_{y_j}^{y_{j+1}} \psi_2(u) dx dy \in \mathbb{R}^{p_2} \quad (127)$$

Then we see

$$L = \Psi_1^T \Psi_1 \quad (128)$$

$$M = \Psi_2^T \Psi_2 \quad (129)$$

$$\gamma = \Psi_1 \alpha \quad (130)$$

and

$$\delta = \Psi_2 \beta \quad (131)$$

With this, we may rewrite 114 as:

$$C(\gamma, \delta) = \|\Psi_1^T \gamma - \Psi_2^T \delta + y\|^2 + \lambda_1 \gamma^T \gamma + \lambda_2 \delta^T \delta \quad (132)$$

## H Experiments with the quasilinear PDE

In our experiments, we use an explicit kernel for  $k_1$  and  $k_2$  given by 100 random Fourier features for each of  $\alpha$  and  $f$ . This allows us to simplify the regression problem (114) to a 200-dimensional one. Although the number of random Fourier features was fixed in all experiments, the error decreased roughly in proportion to the inverse of the total number of samples (as can be seen by the slope of the plot in figure 3). Our method allows us to solve the problem in a fixed-size solution space. Plots of  $f(u(x, y))$  and  $\alpha(x)$  and their errors are presented in Figure 3.

## References

- [1] Haim Avron, Michael Kapralov, Cameron Musco, Christopher Musco, Ameya Velingker, and Amir Zandieh. Random fourier features for kernel ridge regression: Approximation bounds and statistical guarantees. In *International conference on machine learning*, pages 253–262. PMLR, 2017.
- [2] Joseph Bakarji, Kathleen Champion, J Nathan Kutz, and Steven L Brunton. Discovering governing equations from partial measurements with deep delay autoencoders. *arXiv preprint arXiv:2201.05136*, 2022.
- [3] Hubert Baty. Solving stiff ordinary differential equations using physics informed neural networks (pinns): simple recipes to improve training of vanilla-pinns. *arXiv preprint arXiv:2304.08289*, 2023.
- [4] Steven L Brunton, Joshua L Proctor, and J Nathan Kutz. Discovering governing equations from data by sparse identification of nonlinear dynamical systems. *Proceedings of the national academy of sciences*, 113(15):3932–3937, 2016.
- [5] Steven L Brunton, Joshua L Proctor, and J Nathan Kutz. Sparse identification of nonlinear dynamics with control (sindyc). *IFAC-PapersOnLine*, 49(18):710–715, 2016.
- [6] Shengze Cai, Zhiping Mao, Zhicheng Wang, Minglang Yin, and George Em Karniadakis. Physics-informed neural networks (pinns) for fluid mechanics: A review. *Acta Mechanica Sinica*, 37(12):1727–1738, 2021.
- [7] Shengze Cai, Zhicheng Wang, Sifan Wang, Paris Perdikaris, and George Em Karniadakis. Physics-informed neural networks for heat transfer problems. *Journal of Heat Transfer*, 143(6), 2021.

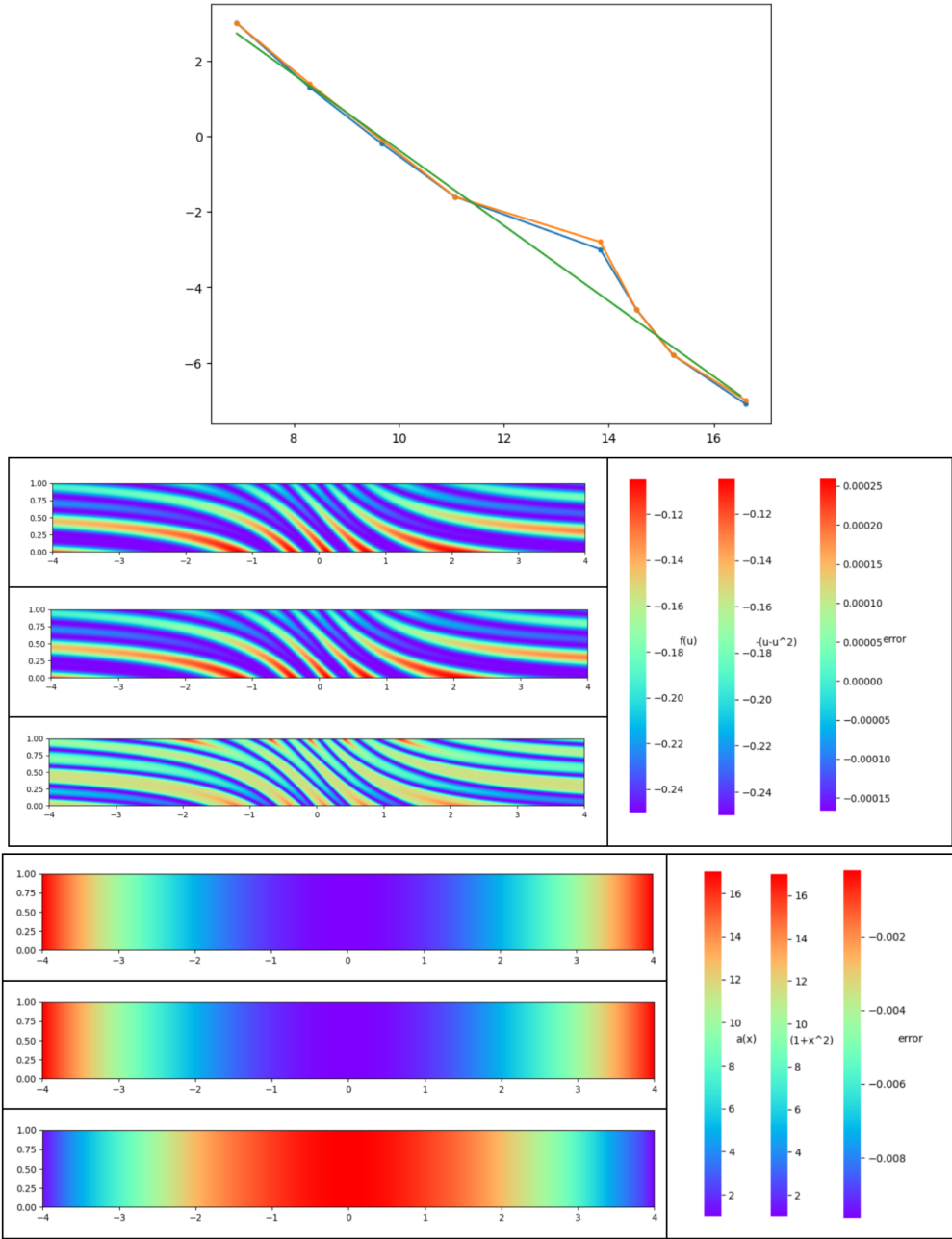


Figure 3: **Top:** Error of  $\alpha$  in orange, and  $f$  in blue. A line with slope of negative one is plotted in green. The error is reported as  $\|f' - f\|_1 / \|f\|_1$  where  $f'$  is the predicted function,  $f$  is the true function, and  $\|\cdot\|_1$  is the  $l_1$  norm. The errors, as a function of the number of observations are reported on a log-log scale.

**Middle:** Prediction  $f(u(x, y))$  over the  $x y$  grid at the top, the ground truth in the middle, and the difference in the prediction and the ground truth is at the bottom. On the right, we present the scales for each of the three plots.

**Bottom:** Prediction  $\alpha(x)$  over the  $x y$  grid at the top, the ground truth in the middle, and the difference between the prediction and the ground truth is at the bottom. On the right, we present the scales for each of the three plots.

- [8] Kathleen Champion, Bethany Lusch, J Nathan Kutz, and Steven L Brunton. Data-driven discovery of coordinates and governing equations. *Proceedings of the National Academy of Sciences*, 116(45):22445–22451, 2019.
- [9] Brian M de Silva, Kathleen Champion, Markus Quade, Jean-Christophe Loiseau, J Nathan Kutz, and Steven L Brunton. Pysindy: a python package for the sparse identification of nonlinear dynamics from data. *arXiv preprint arXiv:2004.08424*, 2020.
- [10] Anthony M DeGennaro and Nathan M Urban. Scalable extended dynamic mode decomposition using random kernel approximation. *SIAM Journal on Scientific Computing*, 41(3):A1482–A1499, 2019.
- [11] Urban Fasel, J Nathan Kutz, Bingni W Brunton, and Steven L Brunton. Ensemble-sindy: Robust sparse model discovery in the low-data, high-noise limit, with active learning and control. *Proceedings of the Royal Society A*, 478(2260):20210904, 2022.
- [12] Richard FitzHugh. Impulses and physiological states in theoretical models of nerve membrane. *Biophysical journal*, 1(6):445–466, 1961.
- [13] Gabriel S Gusmão, Adhika P Retnanto, Shashwati C Da Cunha, and Andrew J Medford. Kinetics-informed neural networks. *Catalysis Today*, 2022.
- [14] Kaiming He, Xiangyu Zhang, Shaoqing Ren, and Jian Sun. Deep residual learning for image recognition. In *Proceedings of the IEEE conference on computer vision and pattern recognition*, pages 770–778, 2016.
- [15] Markus Heinonen, Cagatay Yildiz, Henrik Mannerström, Jukka Intosalmi, and Harri Lähdesmäki. Learning unknown ode models with gaussian processes. In *International Conference on Machine Learning*, pages 1959–1968. PMLR, 2018.
- [16] Sterling C Johnson, Rebecca L Kosciak, Erin M Jonaitis, Lindsay R Clark, Kimberly D Mueller, Sara E Berman, Barbara B Bendlin, Corinne D Engelman, Ozioma C Okonkwo, Kirk J Hogan, et al. The wisconsin registry for alzheimer’s prevention: a review of findings and current directions. *Alzheimer’s & Dementia: Diagnosis, Assessment & Disease Monitoring*, 10:130–142, 2018.
- [17] Kadierdan Kaheman, J Nathan Kutz, and Steven L Brunton. Sindy-pi: a robust algorithm for parallel implicit sparse identification of nonlinear dynamics. *Proceedings of the Royal Society A*, 476(2242):20200279, 2020.
- [18] Kamel Lahouel, Michael Wells, David Lovitz, Victor Rielly, Ethan Lew, and Bruno Jedynek. Learning nonparametric ordinary differential equations: Application to sparse and noisy data. *arXiv preprint arXiv:2206.15215*, 2022.
- [19] Ethan Lew, Abdelrahman Hekal, Kostiantyn Potomkin, Niklas Kochdumper, Brandon Hency, Stanley Bak, and Sergiy Bogomolov. Autokoopman: A toolbox for automated system identification via koopman operator linearization. In *International Symposium on Automated Technology for Verification and Analysis (ATVA)*, 2023. Under review.
- [20] Yunzhu Li, Hao He, Jiajun Wu, Dina Katabi, and Antonio Torralba. Learning compositional koopman operators for model-based control. *arXiv preprint arXiv:1910.08264*, 2019.
- [21] Edward N Lorenz. Deterministic nonperiodic flow. *Journal of atmospheric sciences*, 20(2):130–141, 1963.
- [22] E.N. Lorenz. *Predictability: a problem partly solved*. PhD thesis, Shinfield Park, Reading, 1995 1995.
- [23] Lu Lu, Xuhui Meng, Zhiping Mao, and George Em Karniadakis. Deepxde: A deep learning library for solving differential equations. *SIAM review*, 63(1):208–228, 2021.
- [24] Bethany Lusch, J Nathan Kutz, and Steven L Brunton. Deep learning for universal linear embeddings of nonlinear dynamics. *Nature communications*, 9(1):4950, 2018.

- [25] Daniel A Messenger and David M Bortz. Weak sindy for partial differential equations. *Journal of Computational Physics*, 443:110525, 2021.
- [26] Peter Moczo, Jozef Kristek, and Ladislav Halada. The finite-difference method for seismologists. *An Introduction*, 161, 2004.
- [27] Maziar Raissi, Paris Perdikaris, and George E Karniadakis. Physics-informed neural networks: A deep learning framework for solving forward and inverse problems involving nonlinear partial differential equations. *Journal of Computational physics*, 378:686–707, 2019.
- [28] Joel Rosenfeld. The bahamas, occupation kernels, and system identification.
- [29] Joel A Rosenfeld, Rushikesh Kamalapurkar, Benjamin Russo, and Taylor T Johnson. Occupation kernels and densely defined liouville operators for system identification. In *2019 IEEE 58th Conference on Decision and Control (CDC)*, pages 6455–6460. IEEE, 2019.
- [30] Joel A Rosenfeld, Benjamin Russo, Rushikesh Kamalapurkar, and Taylor T Johnson. The occupation kernel method for nonlinear system identification. *arXiv preprint arXiv:1909.11792*, 2019.
- [31] Benjamin P Russo, Rushikesh Kamalapurkar, Dongsik Chang, and Joel A Rosenfeld. Motion tomography via occupation kernels. *arXiv preprint arXiv:2101.02677*, 2021.
- [32] Mirac Suzgun, Yonatan Belinkov, and Stuart M Shieber. On evaluating the generalization of lstm models in formal languages. *arXiv preprint arXiv:1811.01001*, 2018.
- [33] Jonathan H Tu. *Dynamic mode decomposition: Theory and applications*. PhD thesis, Princeton University, 2013.
- [34] Matthew O Williams, Ioannis G Kevrekidis, and Clarence W Rowley. A data-driven approximation of the koopman operator: Extending dynamic mode decomposition. *Journal of Nonlinear Science*, 25:1307–1346, 2015.
- [35] Enoch Yeung, Soumya Kundu, and Nathan Hodas. Learning deep neural network representations for koopman operators of nonlinear dynamical systems. In *2019 American Control Conference (ACC)*, pages 4832–4839. IEEE, 2019.
- [36] Yong Yu, Xiaosheng Si, Changhua Hu, and Jianxun Zhang. A review of recurrent neural networks: Lstm cells and network architectures. *Neural computation*, 31(7):1235–1270, 2019.